5-1-2018

Effects of Free-stream Turbulence on Tidal Turbine Blade Performance and Wake

Angela Marie Lawrence
Lehigh University, angelawrence11@gmail.com

Effects of Free-stream Turbulence on Tidal Turbine Blade Performance and Wake

by

Angela Lawrence

A Thesis

Presented to the Graduate and Research Committee

of Lehigh University

in Candidacy for the Degree of

Master of Science

in

Department of Mechanical Engineering

Lehigh University

Bethlehem, PA – 18015

May 2018

Approval Sheet

This thesis is accepted and approved in partial fulfillment of the requirements for the Master of Science in Mechanical Engineering.

Effects of Free-stream Turbulence on Tidal Turbine Blade Performance and Wake

Angela Lawrence

_____

Date Approved

_____

Dr. Arindam Banerjee

Thesis Advisor & Associate Professor,

Department of Mechanical Engineering & Mechanics

Lehigh University

_____

Dr. Gary Harlow

Department Chair Person

Department of Mechanical Engineering & Mechanics

Lehigh University

Acknowledgements

I would like to express my sincere gratitude to my thesis advisor, Dr. Arindam Banerjee, for his guidance, instruction, and support over the course of my Master's research. Special thanks are due to Ashwin Vinod for taking on the role of mentor. He's worked tirelessly since I've known him to progress every project in the lab, and mine would never have been successful without his guidance. I am grateful to Richard Towne (Machinist, MEM) for his assistance in the design and manufacturing of the experimental apparatus. His expertise, insight, and advice contributed significantly to this project's success. I would also like to thank all of my fellow lab members. Several have come and gone through the course of the project, but Zach Farley, Rinosh Polavarapu, Rahul Raghavendra, Sudharsan Kalidoss, Andrew Auvil, and Pranav Modali have remained constant throughout in their help and support. I'd like to thank my parents, Chris and Joann Herms, for their love and support through the entirety of my education. Finally, I need to express my utmost gratitude to my closest friends, Christopher Garman and Kenji Harada. They've done nothing but inspire me, encourage me, and support me from the first day I met them both. My greatest success thus far is in having such a wonderful group of people in my life. I'm eternally grateful to everybody who has helped me in this journey.

Table of Contents

List of Figures

List of Tables

Abstract

Tidal turbines operate inflow conditions with elevated levels of free-stream turbulence (FST) that affect the loads acting on components, which in turn affects the performance. The current work focuses on the use of controlled laboratory experiments to investigate the effects of free-stream turbulence on an SG-6043 turbine blade section. Elevated levels of FST are generated using an active grid generator at turbulence intensities (T_i) varying between 1.5-18%. It was observed that elevated levels of FST increased the coefficient of lift (C_L) and caused a subsequent delay in flow separation. In addition, the coefficient of drag (C_D) also increases at high angles of attack in elevated levels of FST, leading to a reduction in hydrodynamic performance. The measured standard deviations indicate that elevated FST leads to considerable fluctuations in measured forces, which in turn will accelerate fatigue damage to the blade. We report our findings of experiments conducted with the hydrofoil over a broader range angles of attack at various turbulence intensities. Acoustic Doppler Velocimetry measurements are made at several downstream locations to provide insight into the flow mechanism that causes a delay in separation observed at higher values of T_i (3.74-9.20%). Characteristics of the wake downstream of the blade are also discussed. A Blade Element Momentum analysis was performed to evaluate the performance of a model marine current turbine at different FST levels. It was observed that elevated levels of FST led to higher values of C_p at lower TSR with a shift in TSR corresponding to maximum C_p value, a result of direct contradiction with reported experiments. The results are discussed and provide the capability for a BEM method to capture the effect of free-stream turbulence accurately.

1 Introduction

1.1 Importance of Hydrokinetic Energy

Alternative methods of harvesting energy become more and more critical as the world energy crisis worsens. Non-renewable resources such as coal, oil, and natural gas are becoming too scarce for the energy demand required, and current renewable resources are not sufficient or cost-efficient to replace older methods. Hydropower is one of the most reliable natural sources of power generation as it does not face challenges like time of day (as solar does), or wind temperament (as the wind does). Within the umbrella category of hydropower, there are hydrostatic devices and hydrokinetic devices. Hydrostatic is the more traditional method of hydropower, in which water is pumped into a reservoir. This is done so that potential energy may be extracted from the pressure head using turbomachinery [1]. This paper deals directly with hydrokinetic devices, in which kinetic energy in a flow is directly converted into electricity by much smaller scale devices [2]. Hydrokinetic devices are currently extremely under-utilized. There is potential in the United States alone for hydrokinetic energy to generate up to 250 Terawatt hours per year of power. As such, we've chosen to focus on characterizing flow around and performance of marine hydrokinetic (MHK) devices according to the harsh environments for which they're intended.

1.2 Performance of Devices

The development of marine and hydrokinetic energy for broad commercial use gives rise to numerous technical challenges and opportunities. One of the key challenges has been survivability and reliability of devices operating in the corrosive marine environment. When devices are tested in laboratory settings, the flow is typically

laminar and has no suspended sediment. In reality, the flow in a body of water would be turbulent due to the presence of rocks and such, would have a boundary layer from dirt and sand over which the water is flowing, and would have particles suspended in the water that corrode the blades. All of this decreases the life of a turbine that has been placed in water. As such, it is necessary to design turbines with vast factors of safety to account for the unpredictability of these factors. Success stories of hydrokinetic devices are, therefore, primarily due to over-engineered solutions that increase both development and maintenance cost.

1.2.1 Effect of Turbulence on Hydrokinetic Turbines

One topic that has received little consideration to date is the impact of turbulence on the performance and loadings acting on a tidal turbine and its many components[3-9]. Turbulence describes the chaotic motions within a fluid flow and can result in fluctuations in force, which is detrimental to the fatigue life of the turbine. In recent years, several studies have reported the characteristics of the tidal flow (consisting of cyclical mean flow and elevated levels of turbulence intensity – henceforth referred to as FST) at tidal energy sites in the UK [10] and in the US[11, 12]. The turbulence intensity was found to be relatively constant over the tidal cycle at approximately 12-13% in the stream-wise directions and 9-10% and 7-8% respectively in the transverse and vertical directions. Table 1 indicates measured turbulence intensities at potential tidal sites that are available in the literature.

Table 3: Turbulence intensities measured at various potential hydrokinetic launch points.

Locations	U (m/s)	T_i (%)
Fall of Warness, U.K. [13, 14]	1.5	7.9-8.7
Sound of Islay, U.K. [10]	2.0	9.5-10.3
Puget Sound, WA, U.S. [12]	1.3(±0.5)	6.6/9.0
Strangford Narrows [15]	1.5-3.5	4-9
East River, NY, U.S. [11]	1.5-2.3	16-24

In their facility, Blackmore et al. [3] tested a model turbine with T_i ranging from ~5-15% using passive generators. They suggested that the turbine power output fluctuations were indicative of the load experienced by the blade, which provides an indicator that maintenance may be necessary. Mycek et al. [5] generated T_i of ~15% by removing the honeycomb structure from the recirculating water tunnel and used this setup to test a model turbine for the effect of turbulence. They observed that turbulence had little effect on the mean loads experienced by individual turbines; however, it altered the magnitude of the velocity deficit in the downstream wake, which would have effects on second-row turbines. Based on wind tunnel studies to test the effect of FST on wind turbines, potential effects of turbulence on turbines in a farm setting could also include increased lift coefficient, an improved lift to drag ratio[16], a significant increase in stall angle [17], and strong leading edge vortices [18]. Wind tunnel experiments on airfoils for micro-air vehicles in high levels of turbulence demonstrate enhanced separation that is expected at angles of attack >25° [18].

1.3 Experiments to Investigate Performance

1.3.1 Grid

Typical laboratory water tunnels use flow-conditioning methods, which lead to laminar free-stream with T_i of the order of ~ 1-3%[3, 5, 19]. Various turbulence-generating mechanisms have been developed for use in laboratory testing and can be classified into two overarching categories: passive generators and active generators. Passive generators are entirely stationary. They are grids constructed in such a way that the flow is perturbed to a particular turbulence intensity at a specific velocity. There is no way to maintain velocity and adjust the turbulence intensity with a passive grid. Instead, a different grid must be used to generate a different level of turbulence intensity. Overall, there is little control of turbulence intensity available with a passive grid, which makes it difficult to investigate the various real-life scenarios that a hydrokinetic device may experience. Experiments to determine the effect of FST on tidal turbines are few, and all the studies are restricted to passive generation techniques[3, 5]. An active grid, on the other hand, has a series of flapping winglets that may be moved in different patterns (or fixed at different orientations) to produce different levels of turbulence intensity at the same velocity. Active grids have historically been used in wind tunnels [20-22], but the implementation of a specially designed tunnel section for inserting and removing the active grid in the Lehigh water tunnel allowed for a water-based active grid to be used. Our active grid allows much broader control on the properties of seeded free-stream turbulence which would allow investigation of a broad range of turbulence parameters that are encountered in installation sites.

1.3.2 Blade Experiments

In this research, we have performed the first reported experiments where free-stream turbulence (FST) is generated with an active grid type turbulence generator in a water tunnel, which allows for higher generated levels of turbulence. Experiments reported involving the testing of a blade section employed for a tidal turbine [23]. The objective of this paper is two-fold. We first determine the lift and drag forces acting on a tidal turbine blade section at various angles of attack under both laminar and turbulent free-stream conditions. The measured hydrodynamic data sets are then used in a Blade Element Momentum analysis to evaluate the coefficients of power and thrust for a tidal turbine subjected to elevated levels of free-stream turbulence. Furthermore, the wake velocities behind the blade are measured at various points downstream to better characterize the flow around the blade.

2 Methods and Experimental Setup

2.1 Experimental Medium

2.1.1 Tunnel

All experiments are performed in the open surface recirculating water channel at Lehigh University (Bethlehem, PA, USA). Refer to figure 1 for the general test setup. The test section is 0.61m wide, 0.61m tall and 1.98m long and is capable of attaining a maximum flow velocity of 1 m/s.

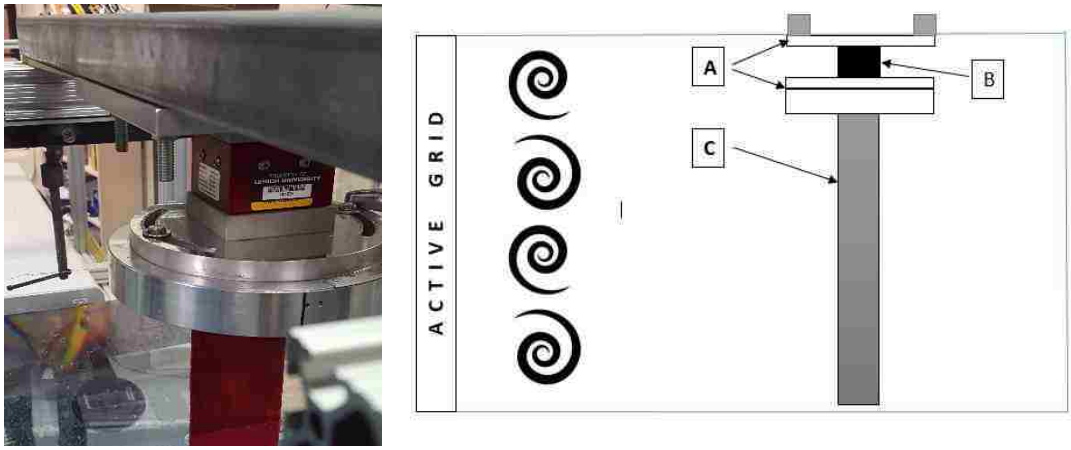

Figure 1: General test setup for hydrofoil experiments (physical and model). In the model, 'A' is the structural support holding up the hydrofoil, 'B' is the Futek sensor that is taking load measurements, and 'C' is the hydrofoil.

2.1.2 Active Grid

Gad-el-Hak & Corrsin [24] defined a dynamic generator as one that has moving boundaries or adds a mean momentum to a turbulent flow. Any design that does not comply with the above definition is considered a passive generator. The turbulence generator developed in-house (see figure 2) is a Makita type active grid [25-27]. It is comprised of ten shafts with attached winglets, of which five are horizontal, and five are vertical. The grid cross-sectional area is 0.61m × 0.61m that mates with the test

section entrance of the tunnel with a length of 0.15m. The winglet shafts are 0.01m in diameter and have six winglets each. The square winglets are each 0.06m on each side and are fastened to the shafts with their diagonals aligned with the shaft, in a diamond fashion. The shafts are arranged in a bi-planar configuration with all the vertical shafts in one plane and all the horizontal shafts in another, spaced 0.01m apart from each other and symmetric about the center of the active grid module. These winglets rotate in at varying speeds and in varying directions to generate elevated levels of free-stream turbulence. Each winglet shaft is controlled by a 23 NEMA series, 23MDSI stepper motor (Anaheim Automation) which includes an onboard simple controller/indexer and a micro-stepping driver. It runs off a 12-24VDC supply with a max power intake of 40W and is capable of generating up to 230oz-in of torque. The RS485 communication protocol is used and commands accepted at a baud rate of 38400 bits per second. In our experiments, the motors are operated at 1600 steps/revolution, giving a resolution of 0.225^{o}. In addition to the 60 rotating winglets, the grid is also fitted with 24 fixed half-winglets, upstream of the plane of the rotating winglets, along with the inner perimeter of the active grid frame. In order to ensure the absence of water leakage and minimum shaft friction, PTFE V-ring seals are used at the shaft ends closer to the motors. The tunnel was operated at a fixed mean upstream velocity of 0.86 ± 0.02 m/s for all wing experiments reported in this paper.

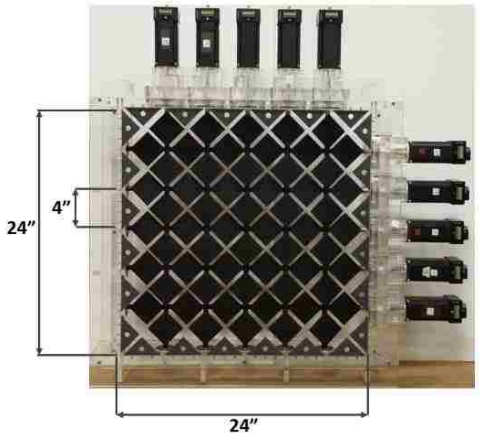

Figure 2: Lehigh active grid turbulence generator

Previous studies with active grid turbulence generators have used different forcing parameters/operating protocols that define the dynamic behavior of the system. The three most common protocols in active turbulence generation are synchronous (SN), single random (SR) and Double random (DR). In the SN protocol, each winglet shaft rotates at a constant (user-defined) velocity. This produces smaller turbulence levels, the slower downstream decay of turbulence kinetic energy, and reduced lateral homogeneity. The properties of FST are found to be highly correlated with the initial position of the rotating winglets. Makita & Miyamoto [26], Mydlarski & Warhaft [22] and Poorte & Biesheuvel [28] reported distinctive spikes in the energy spectrum in the lower frequency range, which was caused due to the large periodicities in the generated turbulence due to the periodic grid rotation. On the contrary, the SR protocol attempts to excite the lower frequencies in the spectrum uniformly by keeping the angular velocity constant while switching the direction of rotation of the winglet shafts at random intervals. The time traveled without a change in rotational direction or speed

(called the cruise time) is varied randomly between a predetermined minimum and maximum value. Increased Ti and lateral homogeneity have been reported with the SR protocol. The peaks in the lower frequency region of the energy spectrum are still observed, however with a smaller magnitude[22]. The DR protocol introduced by Poorte & Biesheuvel [28], randomizes all three parameters, including cruise time, rotational speed, and direction. The authors found that they could change the macro structure of turbulence through the resulting integral time scale by choosing speed and cruise time. The spike in energy spectrum observed with the other protocols was not seen using the double random profile, and the isotropy and turbulence intensities were high [28]. The forcing protocols were programmed using LabVIEW. The schematic of the protocols is shown in figure 3.

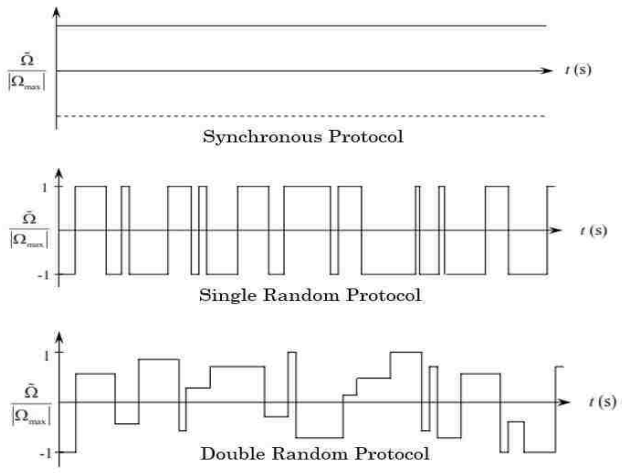

Figure 3: Schematic of active grid operating protocols

The turbulent velocity field generated by the active grid was analyzed using the Acoustic Doppler Velocimetry (ADV) technique. Measurements were taken horizontally across half of the tunnel every inch. These values were then mirrored across

the center of the tunnel (due to the symmetry of the tunnel). Data were collected at each point at 20Hz for 30 seconds. This allowed for convergence in the data. The turbulence intensity was measured as

$$T_i = 100\sqrt{\frac{\sigma^2(u') + \sigma^2(v') + \sigma^2(w')}{3(U_\infty^{\,2} + V_\infty^{\,2} + W_\infty^{\,2})}} \qquad (1)$$

where U_∞, V_∞, and W_∞ are the time-averaged velocity components along the three coordinate directions and u', v' and w' are the corresponding instantaneous velocity fluctuations that represent the variance of the corresponding fluctuating velocity component. A convergence study that monitored the time-averaged velocity and the root mean square velocity fluctuation was performed to ensure that the statistics remained stationary concerning sampling time. Four free-stream conditions were chosen for testing the wing. They are, respectively:

- T_i = 1.5% produced without the active grid (referred to as laminar free-stream);
- T_i =3.74% produced when the active grid was completely open (but not running);
- T_i = 6.65% that was produced with the winglets fixed at a position of 60º from the horizontal (but not operating);
- T_i = 9.2% produced with the active grid operating in a double random mode with rotation frequency randomly varying between +1 and -1 Hz (‘+’ denoting counter clockwise and ‘–‘ denoting clockwise rotational directions)

Blockage created by the grid makes it necessary to characterize the velocity of the tunnel. This ensures that the mean velocity is the same between different tests (despite different turbulence intensities) and that the boundary layer created by the wall of the tunnel is identified and defined. Measurements are not to be made within

two inches of the walls or floor of the tunnel. The velocity measurements at each T_i at different locations across the width of the tunnel (normalized by the chord length, *c*), is plotted in figure 4. Measurements were made in only one quadrant of the cross-section of the tunnel and mirrored over the major axis to provide a full depiction of the velocity profile. All measurements were taken at ten meshes downstream.

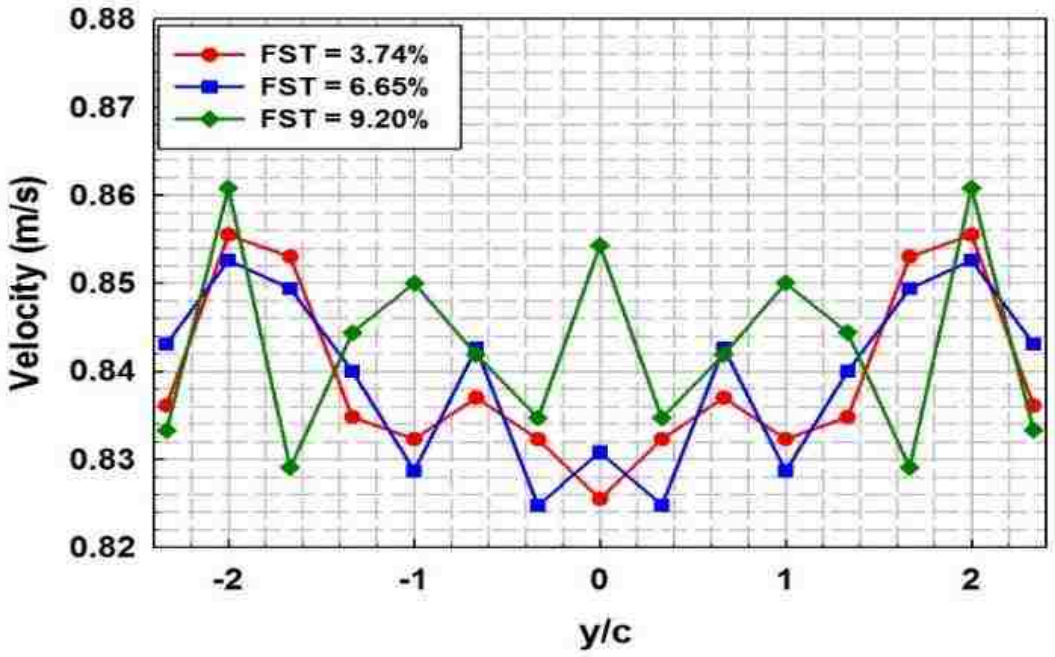

Figure 4: Horizontal velocity distribution of the water tunnel.

2.2 Wing Experimental Model

Our turbine blades have an SG6043 cross-section [23, 29, 30]. It is characterized by its 10% thickness and 5.5% camber. It was developed by Seig and Giguere [31] for small variable-speed wind turbines with a rated power of 1-5KW. It was designed to be operated at a chord-based Reynolds number of $\sim 3\times10^5$ and is known to produce a coefficient of power (C_p)~ 0.37 [23]. Original models of the wing

used in past experiments within the group were manufactured in one part and were made of either plastic or aluminum. However, the plastic wing used had a slightly larger chord length and was extremely subject to bending under the force of the flow. The aluminum blade was sturdy, and not subject to bending at all. However, it's chord length was 8 inches, which prevented measurements at higher angles of attack from being taken. As the blade reached these higher angles of attack, the blockage in the tunnel increased to unacceptable levels that accelerated the flow on either side of the wing, affecting the results of the measurements. To improve the quality of the measurements, it was necessary to design a smaller blade, as this would reduce the solid blockage during measurements. Originally, this was attempted by 3D printing hydrofoil sections on an Ultimaker 3D printer. These were designed in Solidworks (figure 5), 3D printed and then attached by running a thin rod through the middle to provide a structure that the previous plastic wing was lacking, and compressed with nuts on either side of the rod. The entire blade was coated in XTC 3D, which is a lacquer-type substance for 3D printed parts. This coated the parts and gave them an even surface finish so that the uneven texture of the finished print would not affect the measurements. However, this blade experienced too much bending, despite the rod running down the center. Therefore, another technique was employed to 3D print some blade sections out of stainless steel and attach them in the same fashion with the rod in the middle.

The model hydrofoil was built using an additive manufacturing technique called selective laser sintering. In this process, a layer of stainless steel powder is solidified in the appropriate profile using lasers. The hydrofoil was manufactured in

six 4” sections, held together by a unifying rod that runs through the center of the hydrofoil. Figure 5 displays the wing sections just after the process of selective laser sintering, and shows the fully constructed wing, ready for experiments in the tunnel. The profile of the hydrofoil has a chord length of 0.0762m and spans 0.61m (aspect ratio = 8). The span (and, therefore, the aspect ratio) may be decreased by lowering the water level of the tunnel, thereby decreasing the span of the hydrofoil that is in use during any given test. The hydrofoil is mounted on a set of two circular plates that allow it to rotate to different angles of attack when adjusted.

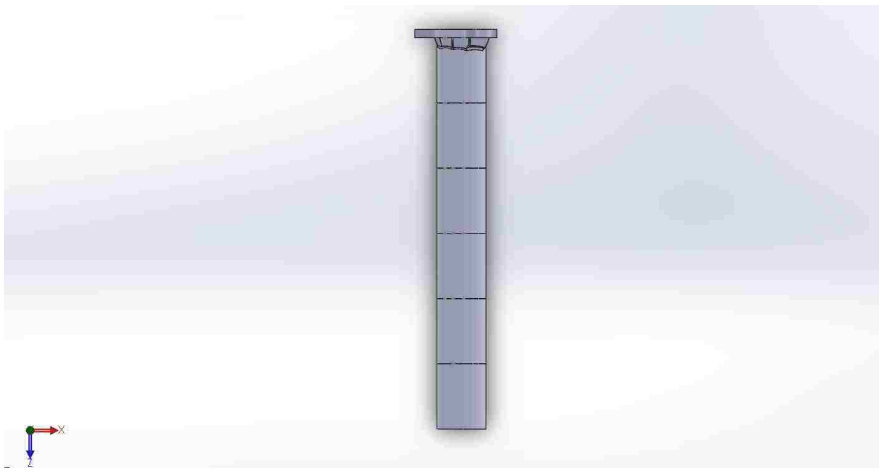

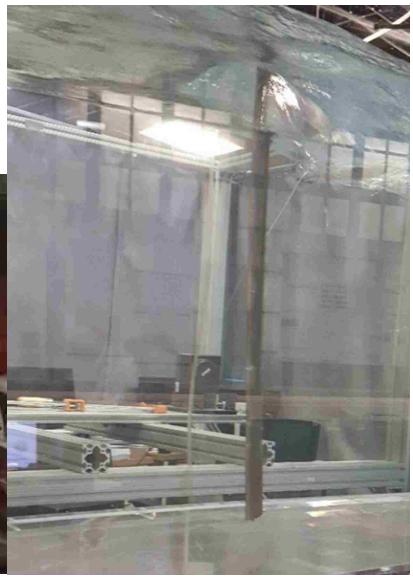

Figure 5: CAD model of the 3D printed wing, Wing sections after selective laser sintering, before they are removed from the base plate and cleaned., Constructed wing section mounted in the tunnel for experiments

2.3 Analytical Methods

2.3.1 BEM

All measurement data was processed using Blade Element Theory and Momentum Theory techniques, which are combined into a Blade Element Code by Manwell. Hydrodynamic performance of a tidal turbine is governed by various operating conditions and blade profile geometry. Blade-element-momentum (BEM)

analysis which forms the backbone of wind turbine rotor design has been used by several developers for tidal turbine designs [32, 33]. BEM theory, originally attributed to Betz [34-36] and Glauert [32] is a combination of blade element theory and momentum theory. According to the blade element theory, forces on a turbine blade can be obtained by dividing the blade into a number of hydrodynamically independent elements [37]. Hydrodynamic forces on these elements are calculated based on local flow conditions using two-dimensional lift-drag data. The forces on each element are then summed together to find total force on the turbine blade. The other part of BEM, known as momentum theory, assumes that the work done by the fluid on the turbine blade creates pressure (or momentum) loss across the rotor plane. Induced velocities in axial and tangential direction can be calculated from this momentum loss; which in turn affects the forces on the turbine blade. Of many factors that contribute to BEM analysis, an important one is characterizing the flow with *a* and *a'.* Axial induction, *a,* is the fractional decrease in wind velocity between the freestream and the rotor plane. This is used to characterize the velocity in the flow that is induced by the rotation of the rotor. Likewise, the angular induction factor (*a'*) determines the wake rotation that will be added to the flow by the rotor motion. If one defines thrust in a turbine as the area of the turbine multiplied by the difference in pressure directly before and after the turbine, it's possible to incorporate both *a* and *a'* into the force. As a result,

$$T = \frac{1}{2}\rho A U^2[4a(1-a)] \qquad (2)$$

Where T is the thrust of the turbine, A is the area of the blades, U is the free stream velocity, and a is the axial induction. This can then be normalized by the dynamic force of the flow to the following equation:

$$C_T = \frac{T}{\frac{1}{2}\rho U^2 A} \qquad (3)$$

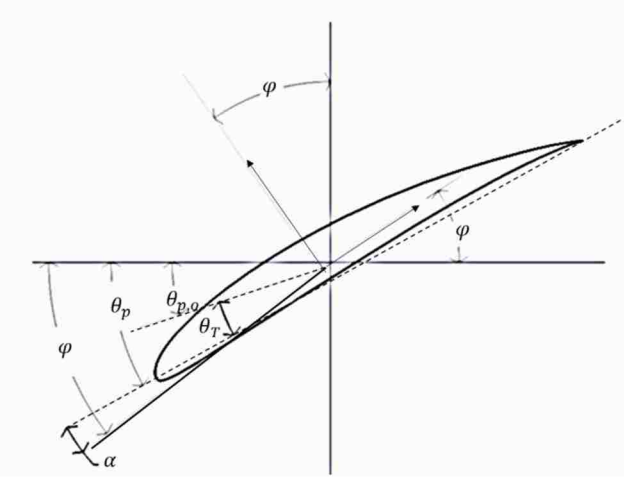

Figure 6: Angles used to describe blade position in Blade Element Momentum code

Based on the blade geometry (figure 6), it is possible to derive relationships between previously determined equations and the geometry of the blade. This predominately means putting the angle of relative wind in terms of *a* and *a'*, which are characteristics of the flow. When calculating the power contribution from each section, we use the equation:

$$dP = \Omega dQ \qquad (4)$$

In this equation, P is power and Q is torque. We may also state that the power is the sum of all the differential powers at each individual element from the root of the blade to the blade tip:

$$P = \int_{R_{hub}}^{R} dP = \int_{R_{hub}}^{R} \Omega dQ \qquad (5)$$

This statement combined with the knowledge that the coefficient of power is, by definition, the power output of the turbine normalized by the power available in the flow allows us to define the following equation:

$$C_p = \frac{P}{P_{wind}} = \frac{\int_{R_{hub}}^{R} \Omega dQ}{\frac{1}{2}\rho\pi R^2 U^3} \qquad (6)$$

We know that dQ is the differential torque and is defined by the following equation:

$$dQ = \frac{B}{2} U_{rel}{}^2 [C_L \sin(\phi) - C_D \cos(\phi)] c r dr \qquad (7)$$

Algebraic manipulation and term grouping allow for recognition of a pre-defined term σ' (where B is the number of blades, R is the turbine radius, and c is the chord length), and simplification of the equation. The final form used of dQ is:

$$dQ = \frac{\sigma' C_L}{\sin(\phi)} (1-a)^2 \rho U^2 [1 - \frac{C_D}{C_L} \cot(\phi)] \pi r^2 \frac{R}{\lambda} d\lambda_r \qquad (8)$$

Finally, this is input into the original C_p equation (equation 6). A number of terms cancel, resulting in the following equation that is used in the Blade Element Code employed in this research. This equation is as follows:

$$C_p = \frac{8}{\lambda^2} \int_{\lambda_r}^{\lambda} \sin^2(\phi)(\cos(\phi) - \lambda_r \sin(\phi))(\sin(\phi) + \lambda_r \cos(\phi))[1 - (\frac{C_D}{C_L}) \cot(\phi)] \lambda_r{}^2 d\lambda_r \qquad (9)$$

In using this equation, a coefficient of pressure is calculated for each element along the blade, and they are all summed together. For the purposes of this paper, it is necessary to use this equation a number of times over a range of tip speed ratios. This

produces a curve of the coefficient of power versus tip speed ratio. This characterizes the performance of a turbine in various conditions.

Just as the coefficient of power is dependent on the differential torque derived from momentum theory, the coefficient of thrust is dependent on the differential normal force derived from momentum theory. The local thrust coefficient for each annular rotor section can be defined as follows:

$$C_{T_R} = \frac{dF_N}{\frac{1}{2}\rho U^2 2\pi r dr} \qquad (10)$$

When the equation for dF_N from momentum theory is subbed back into this equation, it results in the following expression for C_T at a specific element in the blade.

$$C_{T_R} = \frac{\sigma'(1-a)^2 (C_l \cos(\varphi) + C_d \sin(\varphi))}{\sin^2(\varphi)} \qquad (11)$$

All elements may then be summed to determine the total thrust.

2.3.2 Sensitivity Analysis

Due to size restrictions on the wing model, there were issues with bending at high angles of attack that prevented a full range of angles of attack from being collected through experimentation. As a result, a sensitivity analysis was performed to determine what forces would be like at higher angles of attack and to see whether these values had an impact on the solution output by the BEM code. The ideal way to do this would be to perform an analysis on a plate at a 90-degree angle of attack to the flow. However, a standard form of such an analysis does not appear to be typically

performed throughout the literature. Numbers can be derived for an inviscid plate under such conditions, but not a viscid plate. As such, an alternative analysis was performed to determine the magnitude of the effect of the higher angles of attack.

It was first assumed that the changing angle of attack of the blade would simply change the distribution of force between lift and drag. Because lift and drag are perpendicular to each other, it is possible to resolve each of these into one vector that will have approximately the same magnitude for each angle of attack measured. This magnitude, once the calculations were performed was roughly 30 Newtons. We may then perform an analysis where the drag on the wing when the wing is perpendicular to the flow is 30 Newtons. Although this is not an overly scientific method of determining a number that may be used, it does allow for rough estimates to see the sensitivity of BEM to these higher angles of attack. Table 2 shows the percent difference between the BEM results found when the tails of the higher angles of attack were filled with either the force expected on an inviscid flat plate or the forces expected on a viscid flat plate, according to the method described above.

It was determined that the higher angles of the attack had minimal impact on the BEM results. Even when lift and drag measurements at the higher angles of attack were elevated to higher numbers (such as 100 Newtons), the curve barely changed. Even still, further measurements are being performed in which the wing is being secured to the base of the tunnel in attempts to attain measurements at higher angles of attack.

Table 4: Sensitivity analysis of the effect of high angles of attack on BEM results

	PERCENT DIFFERENCE BETWEEN INVISCID FLAT PLATE AND VISCID BEM RESULTS	PERCENT DIFFERENCE BETWEEN CONSTRUCTED FORCE DATA AND VISCID BEM RESULTS
MAX	0.02%	2.33%
AVERAGE	0.00%	-1.4%
MIN	0.01%	-6.0%

2.4 Measurement Techniques

2.4.1 Load Measurements

The wing assembly is attached to a 3-axis Futek load cell (Model# MTA400), which has a measurement uncertainty of 0.25%, which measures all three components of force acting on the hydrofoil model. During performance testing, the end gap between the hydrofoil and the bottom surface of the tunnel is designed to be 0.105" or less, which is 0.005 times the hydrofoil span [38]. This spacing allows the floor of the tunnel to act as an end plate and mitigate tip vortices and other end effects. The hydrofoil is mounted on top of the tunnel with two bracing pieces of channel. All experiments with the blade section were conducted at a Reynolds number of 6.3×10^4, to match conditions for experiments performed with the labs model turbine.

2.4.2 Wake Measurements

The wake of the blade was characterized by laminar free-stream, 3.74% T_i, and 9.20% T_i; at three angles of attack (0º, 12.5º, and 20º). These three angles of attack were chosen to represent pre-stall, stall, and post-stall conditions. All wake velocity measurements were taken with an ADV. Data were collected at two downstream locations (two chord lengths and four chord lengths away from the blade) [16]. The

angle characterized is determined by the separation point seen in each T_i during performance testing. The distribution of force over the hydrofoil does not affect the wake and is therefore inconsequential. As a result, we can distribute some force on the hydrofoil to the tunnel floor by securing it with an industrial strength suction cup. This stiffens the hydrofoil and prevents any potential bending; thereby ensure the true nature of the wake is unperturbed. Furthermore, all measurements are taken at 12 inches above the floor of the tunnel and do not see the effect of the suction cup boundary layer. The wake of the blade was characterized in laminar free-stream (1.5% TI), 6% TI, and 18% TI at two angles of attack (0 degrees and 15 degrees).

2.4.3 Blockage Correcting

It is recommended that solid blockage for lab-scale experiments should be kept below 7.5% [38], to avoid blockage effects impacting lift and drag measurements. A recent study by Maldonado et al. [16] extends this limit to a value of 8.5%. At the angles of attack typically tested for aerodynamic studies (0º to +25º), solid blockage in the experiments performed is well within the limit prescribed. For tidal turbines, the angles of attack that the blade encounters range from -2º to +50º. This range of angles of attack gives a maximum solid blockage of 8.0%. Thus, a blockage correction is not necessary. Experiments at higher angles of attack were not performed at this time as they would require reliable correction methods for blockage in a water channel.

3 Results

3.1 Wing Hydrodynamics

3.1.1 Lift and Drag Measurements

An accurate estimation of hydrodynamic loads acting on the hydrofoils is critical for creating optimal blade designs that enhance the turbine efficiency and the power output under different FST conditions. In each experiment, lift and drag were measured under different turbulence intensities, at different angles of attack. These forces are non-dimensionalized to produce the coefficient of lift, C_L, and the coefficient of drag, C_D:

$$C_L = \frac{L}{\frac{1}{2}\rho U^2 AR} \tag{12}$$

$$C_D = \frac{D}{\frac{1}{2}\rho U^2 AR} \tag{13}$$

where L is the lift force generated, D is the drag force measured, and AR is the planform area of the hydrofoil. The ratio of the lift coefficient and the drag coefficient is used to characterize the efficiency of the hydrofoil [16]. A high lift to drag ratio implies larger kinetic energy capture.

The lift on the hydrofoil was measured in a range of angles of attack under laminar free-stream condition (resulting in T_i ~1.5%). This range of angles of attack is from -40 degrees to 40 degrees, in increments of 5 degrees. More measurements are taken near the stall point to more closely determine the behavior of the blade. Generally, in characterizing blade performance, measurements are only taken from -16 degrees to 25 degrees and are usually taken in wind tunnels [39]. Beyond stall, it's generally accepted

that there will be a drop in the lift and an increase in drag and that it's not necessary to characterize because blades aren't necessarily used at these angles of attack. However, an analysis of the Blade Element Momentum code outlined by Manwell [40] and programmed in previous works within the group [41] suggests that experimental values used in determining the output of the BEM code range from -2 to 50 degrees. Feeding the full range of experimental data that will come into play into the BEM code improves output accuracy. These baseline experiments are compared to the three identical tests run with grid-generated FST, in which the levels of T_i generated are 3.74%, 6.65%, and 9.20%. The amount of lift generated at any given angle of attack correlates directly to the amount of power that a turbine can produce. Figure 7 plots C_L for all four test conditions as a function of the angle of attack. For all test cases, the measured lift value reaches a peak at the stall angle, after which it drops off. In the laminar free-stream case, the maximum coefficient of lift ($C_{L,\,max}$) was 1.73 obtained at the stall angle at 10º.

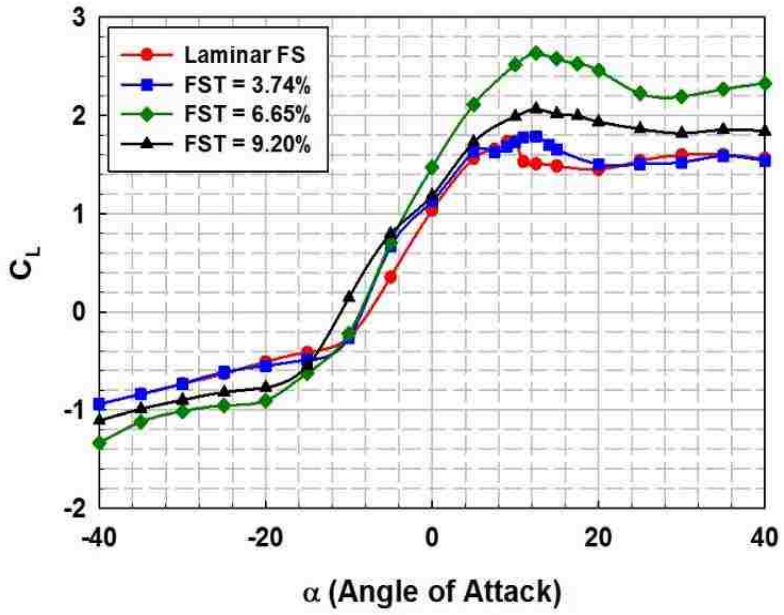

Figure 7: Coefficient of lift as a function of the angle of attack for tested turbulence intensities. The Laminar case corresponds to a Laminar FST with Ti ~ 1.5%.

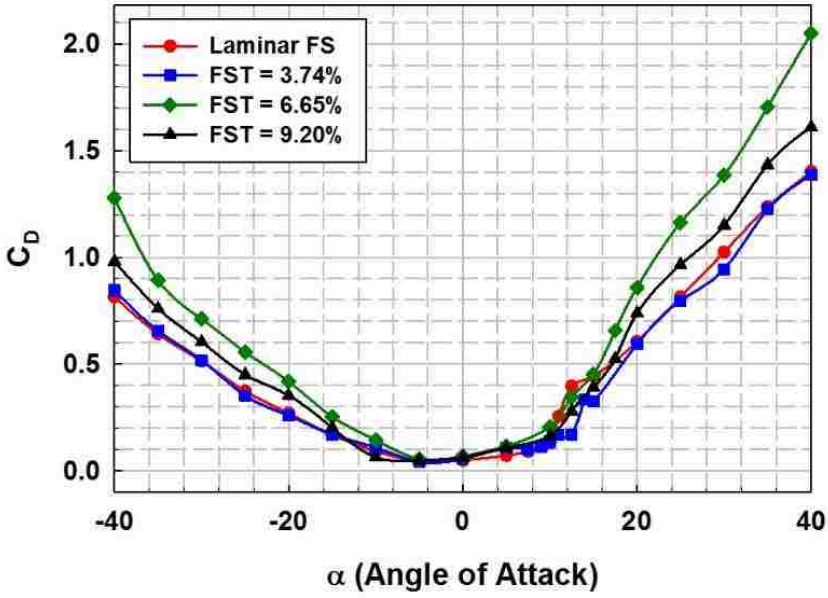

in

Figure 8: Coefficient of drag as a function of the angle of attack for different turbulence intensities tested.

Two trends were identified when comparing the data acquired in the laminar base case. The first of these two trends related to the location of the stall. In all cases with

elevated FST (T_i = 3.74%, 6.65%, and 9.20%), the stall angle was delayed from 10º to 12.5º. To ensure that this trend was accurately noted, measurement resolution around the angle apparent location of maximum lift was increased from 5º increments to 2.5º increments (or as little as 1º increments, in such cases where the peak was not apparent). The second trend that was identified was the effect of turbulence intensity on the magnitude of the coefficient of lift. As previously mentioned, the maximum coefficient of lift was 1.73 in flow with laminar free-stream (T_i ~1.5%). Increasing T_i to 3.74% increased the coefficient of lift to 1.78, and further increasing it to 9.20% increased the coefficient of lift to 2.07. Most interestingly, T_i = 6.65% increased the coefficient of lift to 2.64, which represents a 52.6% increase in coefficient of lift from the laminar free-stream case. While the value of lift at any given angle of attack correlates directly to the amount of power that a turbine can generate, the value of drag indicates the resistance to motion. Figure 8 plots the coefficient of drag (C_D) as a function of the angle of attack in the laminar baseline test, and all three grid-generated turbulence conditions.

The measured coefficient for all the cases tested was lowest when close to an angle of attack of zero; the values are higher as the angle of attack increases. The observed drag coefficient was highest for the Ti =6.65% case, which also corresponds to the highest values of lift coefficients measured. The efficiency for each case can be estimated by calculating the ratio of the lift force to the drag force. A high lift-drag ratio indicates that the amount of lift generated is met with minimal drag, and therefore signifies the efficiency of a set of operational parameters. Figure 9 plots the lift to drag ratio over the range of α tested. There is a slight drop in maximum efficiency in the T_i = 3.74% and

9.20% intensity cases. However, the 6.65% Cl/Cd curve demonstrated peak efficiency close to that of the laminar free-stream case. The maximum C_L/C_D value in the laminar case was 22.07, compared with a C_L/C_D value of 21.91 at an angle of attack 5º before the one in laminar flow.

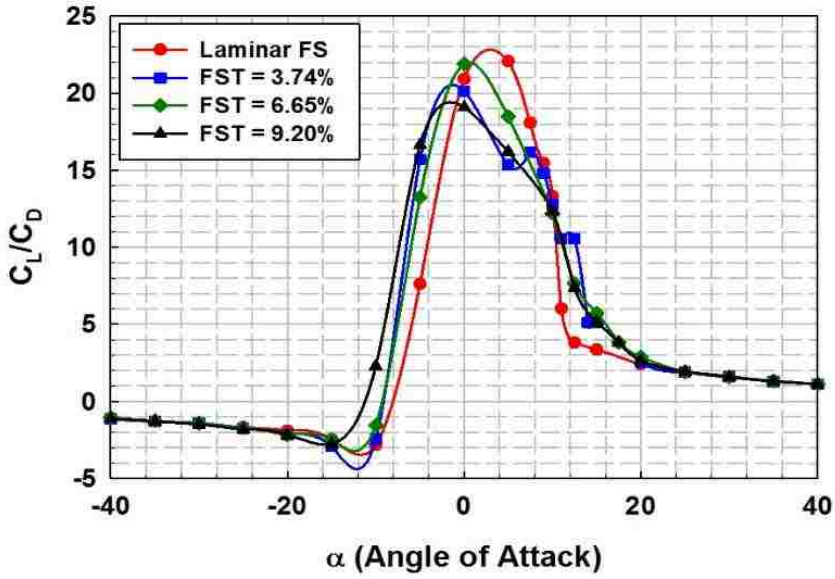

Figure 9: Coefficient of lift divided by coefficient of drag, as a function of the angle of attack, for all tested turbulence intensities. The Laminar case corresponds to a Laminar FST with Ti ~ 1.5%.

3.1.2 Wake Velocity Deficit Measurements

The role of three different turbulence intensities (1.5%, 3.74%, and 9.20%) in the wake of the blade was analyzed at two different locations: two chord lengths downstream, and four chord lengths downstream (where one chord length is three inches). For keeping the number of variables to a minimum, experiments were performed only for the maximum and minimum grid-generated turbulence intensities; our goal is to compare trends in measured quantities due to a factor of 3 variations in turbulence intensity. The velocity measurements are non-dimensionalized using the following:

$$U' = \frac{U_{measured} - U_{\infty}}{U_{\infty}} \qquad (14)$$

where $U_{measured}$ is the wake velocity measured at several points across the tunnel, U_{∞} is the mean free-stream tunnel velocity, and U' is the normalized velocity.

Measurement location in the cross-stream direction (Y) is normalized by the chord length of the blade, C. Upon comparing the two locations downstream for the case of α=0°, it was noted that the wakes are nearly symmetric and that the velocity deficit deteriorated as we moved further downstream of the hydrofoil. Figure 10 plots the wake deficit at each downstream location, demonstrating this trend. The decrease in wake deficit is similar to those documented in experiments with airfoils [42]. As the flow progresses downstream, wake recovery leads to widening of the deficit curve indicating mixing between the wake the turbulent free-stream. The increase in the wake deficit as a function of the angle of attack was evident for all three free-stream conditions, and the wake becomes more asymmetric as the angle of attack increases.

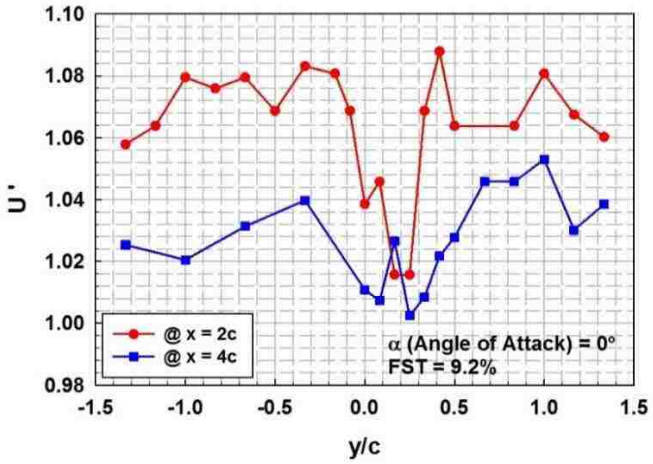

Figure 10: Velocity distribution in the wake at various downstream locations at Ti=9.20% (α = 0°)

Figure 11 plots the results of the T_i=9.20% case, in which all three angles of attack were tested. In the test with α=0°, the wake was skewed slightly to the right, which is expected because the SG6043 is a cambered airfoil. As the α increases to 12.5° however, the wake begins to skew further to the right. This is again due to the geometry of the blade, which redirects the flow to the right. The flow hasn't separated yet at this point. As long as the flow is still attached, the increased angle of attack will skew the wake in this direction. At a 20° angle of attack, the flow is no longer attached.

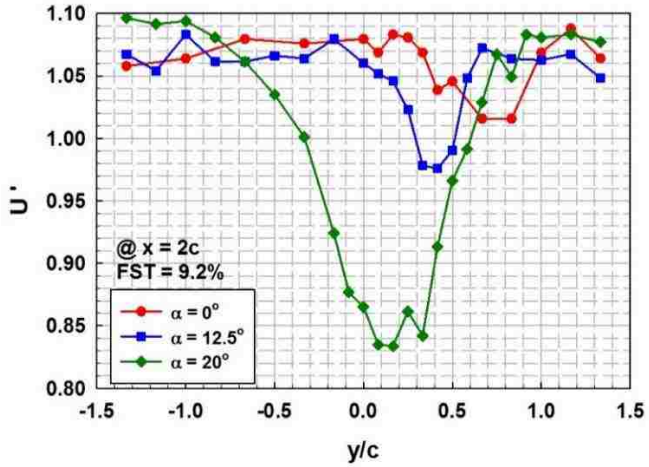

Figure 11: Wake characterization at various angles of attack at 2 chord lengths downstream, Ti=9.20%

The detachment of the wake causes increased turbulence directly behind the blade, which enhances mixing. The increased mixing in the wake of the blade decreases the amount that the wake is skewed to the right by redistributing the energy throughout the flow. Finally, there is an observed increase in velocity deficit that is a direct function of the angle of attack. Increased solid blockage at higher angles of attack decreases the velocity of the flow directly behind the body, thereby accelerating the flow on either side of the hydrofoil. This effect is minimized at the lower angles of attack, in which blockage is low. Similar results were found in all three FST cases, and the 9.20% T_i case

is plotted as it best illustrates the trends at hand. Further analysis was performed by comparing the three FST cases tested.

Figures 15 and 16 illustrate the development of the wake velocity at the three turbulent intensities, at the two locations downstream. Both graphs show an angle of attack of 12.5º. These were compared at 12.5º, as this is closest to stall and therefore the most interesting point in the flow. From the plots of this data (figure 12), it is evident that the laminar free-stream and 3.74% T_i cases have greater deficit two chord lengths downstream of the hydrofoil than the T_i = 9.20% case. This is true for all angles, and at both downstream locations.

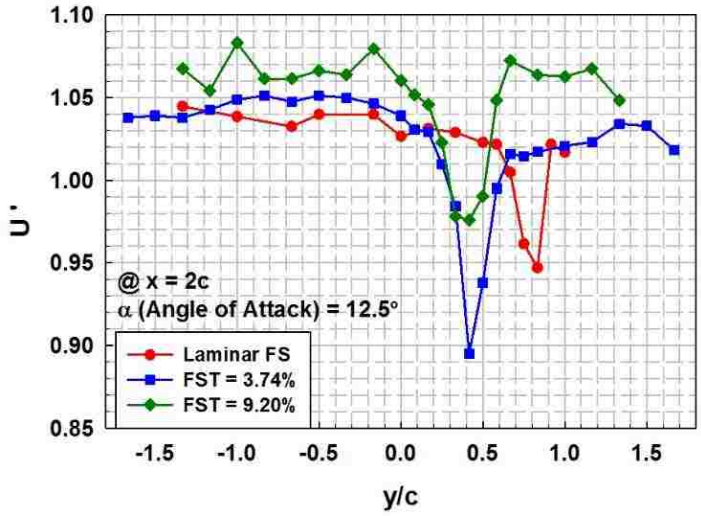

Figure 12: Wake characterization at a 12.5° angle of attack for 2 chord lengths downstream

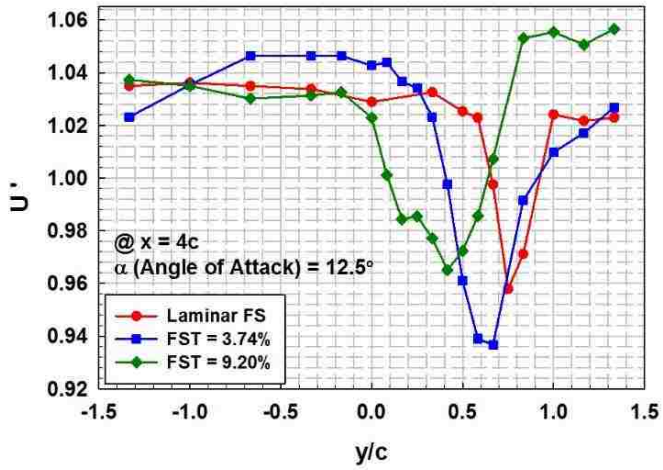

Figure 13: Wake characterization at a 12.5° angle of attack for 4 chord lengths downstream, compared across turbulence intensities

Furthermore, the 9.20% T_i case had a higher average velocity but saw the smallest wake deficit of the three cases. This is due to the increase in cross-stream momentum transfer with more turbulence. There is less deficit in the higher intensity cases because of more mixing. Additionally, the location of minimum velocity in the wake deficit demonstrates the effect of turbulence on the skew. As turbulence intensity increases, more mixing is encouraged across the wake. As a result, the skew in the wake of the laminar free-stream case is slightly less than in the T_i =3.74% case, and further reduced in the T_i =9.20% case. In figure 13, we see the same values plotted at 4 chord lengths downstream, rather than 2. As is the case in figure 12, there is a noticeable decay of the wake in all three turbulence intensities. The wakes in each FST case are still reasonably skewed about the same cross-tunnel location, but the curves have become more broad due to the increased mixing downstream.

3.1.3 Estimating Turbine Performance with a Blade Element Momentum Code

BEM combines blade element and momentum theories and solves coupled equations iteratively to determine fluid forces (thrust and torque) and induced velocities near the rotor [37]. Traditionally, developers obtain hydrodynamic data, i.e., lift coefficient (C_L) and drag coefficient (C_D) for their turbine blades based on available data sets or using Xfoil [43], that calculate lift and drag coefficients for a given hydrofoil by combining a linear-vorticity stream function panel method and a viscous solution method. A surface transpiration model was used to couple a viscous solution (for boundary layer and wake) with an incompressible potential flow solution (for the flow domain away from the turbine surface). BEM formulation developed by our group [29] was used in combination with our measured blade hydrodynamics data to predict the performance of a model turbine. Three data-sets are presented for discussion – Laminar free-stream (no grid case) and elevated FST with T_i of 3.74% and 9.20%. The power coefficient is evaluated using[37] as:

$$C_P = \frac{8}{\lambda^2} \int_{\lambda_{hub}}^{\lambda} \lambda_r^3 a'(1-a)\left[1-\left(\frac{C_D}{C_L}\right)\cot\phi\right] \, d\lambda_r \qquad (15)$$

where a and a' are the axial and angular induction factors, λ_r is the local TSR and Φ is the angle of relative flow. The maximum value of the axial induction factor (a) was kept below 0.5; any value over this point would imply that the flow has reversed downstream of the turbine. The angular indication factor (a') can take any value but was generally small and close to zero; it should be noted that if both values are negative, the

turbine is acting like a propeller[33]. The results from our BEM analysis is plotted in figure 14.

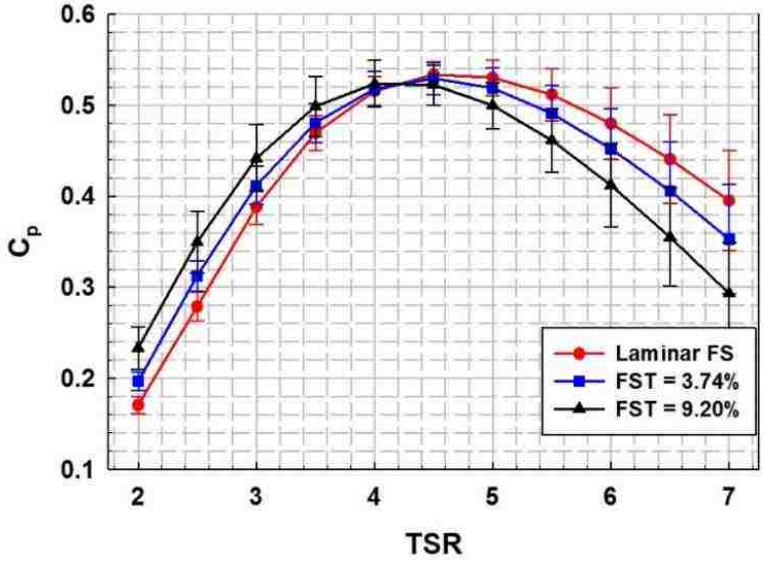

Figure 14: Comparison of turbine power coefficient as a function of tip speed rate for three different inflow turbulence intensity levels

The turbine simulated is a three-bladed, zero twist, model turbine, with the SG6043 wing profile. The pitch angle used was 10º, as previous lab studies have indicated that this is the optimal pitch angle for this turbine [29]. The BEM code was run over a range of $2 \leq TSR \leq 7$ in increments of 0.5. Experimental results for this model turbine are further discussed in a companion paper [44]. An error analysis was also performed, and representative errors in power coefficients of a model turbine are shown for each curve. The BEM analysis shows that elevated levels of FST cause higher values of C_p at lower TSR with a shift in TSR corresponding to maximum C_p value. Upon a cursory glance, this result may appear to be confusing as experiments reported in the literature [3, 5] and those performed in our laboratory (and reported in a companion paper[44]) contradict the BEM findings; the power coefficient is not influenced by the

effect of FST as reported widely. A closer look at eq. (5) explains the discrepancy. Our hydrodynamic measurements result in different values of C_D/C_L for the different FST cases. Thus, the effect of changing FST→ a change of C_D/C_L would be mathematically similar to change the relative angle of flow or the blade pitch angle. The trend of C_p curve observed in figure 17 is similar to results obtained in our previous work [29] where C_D/C_L was held constant (and was based on XFoil), but the blade pitch angle was changed (see fig.7 in ref. [29]). We thus attribute the discrepancy in our BEM estimate to the steady state BEM formulation.

The BEM Prediction for Coefficient of Thrust did not demonstrate results as consistent as those seen in the Coefficient of Power predictions. This is demonstrated in figure 18. Between the 9.20% and 3.74% cases and the laminar, there appears to be a change in slope. This implies that the thrust increases at a faster rate with higher tip speed ratios at higher turbulence intensities. However, the 6.65% case appears to be something of an anomaly. It represents a shift upwards of the laminar free stream case. This suggests higher thrust overall in cases of higher turbulence intensity. Overall, the results of this prediction fail to indicate a trend that may be affected by turbulence intensity. This could be due to small inconsistencies in the data.

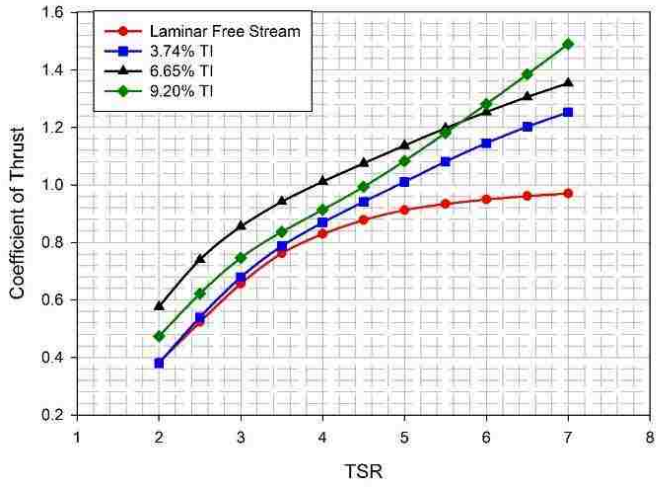

Figure 15: Comparison of turbine thrust coefficient as a function of tip speed rate for three different inflow turbulence intensity levels

4 Concluding Remarks

The experiments discussed in this paper include measuring the load experienced by a blade in flows with elevated free-stream turbulence, measuring the wake behind the blade in similar conditions, and using a simple Blade Element Momentum Code to estimate the effect that free-stream turbulence has on turbines. By using data from the blade in the experimental setup created, we were able to demonstrate a change in expected turbine performance.

- The coefficient of lift increases when the blade is exposed to high levels of FST. However, this does not appear to be a linear increase. It was observed that the 6.65% turbulence intensity increase saw a greater increase in coefficient of a lift than either of the other cases.
- The coefficient of drag increases when the blade is exposed to high levels of FST. When exposed to 3.74% turbulence intensity, there is little change in the

drag experienced by the blade. However, there is a clear increase in drag in the two other turbulence cases, with a higher case in the 6.65% case once again.

- The efficiency of the blade (C_L / C_D) peaks at a higher angle of attack with increased turbulence intensity, which implies that increased turbulence intensity delays the stall angle of the blade.
- Wake measurements indicate that the wake deficit decays downstream of the wing. This is the case for all angles of attack and turbulence intensities, but it was found that an elevated FST can change the location of the center of the wake.
- There is a clear disparity between the BEM results for each of the different turbulence intensities, despite the fact that all conditions that would typically be input to BEM have remained the same. This suggests that turbulence intensity needs to be accounted for in BEM codes. We did this by collecting data on a blade in turbulent flow, but this could also be done by modifying future BEM codes to accept percent turbulence intensity as an input to the code.

References

1. Güney, M. and K. Kaygusuz, *Hydrokinetic energy conversion systems: A technology status review.* Renewable and Sustainable Energy Reviews, 2010. **14**(9): p. 2996-3004.
2. Lago, L., F. Ponta, and L. Chen, *Advances and trends in hydrokinetic turbine systems.* Energy for Sustainable Development, 2010. **14**(4): p. 287-296.
3. Blackmore, T., L.E. Myers, and A.S. Bahaj, *Effects of turbulence on tidal turbines: Implications to performance, blade loads, and condition monitoring.* International Journal of Marine Energy, 2016. **14**: p. 1-26.
4. Bahaj, A. and L.E. Myers, *Shaping array design of marine current energy converters through scaled experimental analysis.* Energy, 2013. **59**: p. 83-94.
5. Mycek, P., et al., *Experimental study of the turbulence intensity effects on marine current turbines behaviour. Part I: One single turbine.* Renewable Energy, 2014. **66**: p. 729-746.
6. Bahaj, A., W. Batten, and G. McCann, *Experimental verifications of numerical predictions for the hydrodynamic performance of horizontal axis marine current turbines.* Renewable energy, 2007. **32**(15): p. 2479-2490.
7. Bahaj, A., et al., *Power and thrust measurements of marine current turbines under various hydrodynamic flow conditions in a cavitation tunnel and a towing tank.* Renewable energy, 2007. **32**(3): p. 407-426.
8. Gaurier, B., et al., *Flume tank characterization of marine current turbine blade behaviour under current and wave loading.* Renewable Energy, 2013. **59**: p. 1-12.
9. Maganga, F., et al., *Experimental characterisation of flow effects on marine current turbine behaviour and on its wake properties.* IET Renewable Power Generation, 2010. **4**(6): p. 498-509.
10. Milne, I.A., et al., *Characteristics of the turbulence in the flow at a tidal stream power site.* Phil. Trans. R. Soc. A, 2013. **371**(1985): p. 20120196.
11. Li, Y., et al. *Inflow measurement in a tidal strait for deploying tidal current turbines: lessons, opportunities and challenges*. in *ASME 2010 29th International Conference on Ocean, Offshore and Arctic Engineering*. 2010. American Society of Mechanical Engineers.
12. Thomson, J., et al., *Measurements of turbulence at two tidal energy sites in Puget Sound, WA.* IEEE Journal of Oceanic Engineering, 2012. **37**(3): p. 363-374.
13. Osalusi, E., J. Side, and R. Harris, *Structure of turbulent flow in EMEC's tidal energy test site.* International Communications in Heat and Mass Transfer, 2009. **36**(5): p. 422-431.
14. Osalusi, E., J. Side, and R. Harris, *Reynolds stress and turbulence estimates in bottom boundary layer of Fall of Warness.* International Communications in Heat and Mass Transfer, 2009. **36**(5): p. 412-421.
15. MacEnri, J., M. Reed, and T. Thiringer, *Influence of tidal parameters on SeaGen flicker performance.* Phil. Trans. R. Soc. A, 2013. **371**(1985): p. 20120247.
16. Maldonado, V., et al., *The role of free stream turbulence with large integral scale on the aerodynamic performance of an experimental low Reynolds number S809 wind turbine blade.* Journal of Wind Engineering and Industrial Aerodynamics, 2015. **142**: p. 246-257.
17. Ravi, S., et al., *Influence of large-scale freestream turbulence on the performance of a thin airfoil.* AIAA journal, 2012. **50**(11): p. 2448-2459.

18. Ravi, S., et al., *The flow over a thin airfoil subjected to elevated levels of freestream turbulence at low Reynolds numbers.* Experiments in fluids, 2012. **53**(3): p. 637-653.
19. Tavoularis, S., *Measurement in fluid mechanics*. 2005: Cambridge University Press.
20. Makita, H. and K. Sassa, *Active turbulence generation in a laboratory wind tunnel*, in *Advances in Turbulence 3*. 1991, Springer. p. 497-505.
21. Kang, H.S., S. Chester, and C. Meneveau, *Decaying turbulence in an active-grid-generated flow and comparisons with large-eddy simulation.* Journal of Fluid Mechanics, 2003. **480**: p. 129-160.
22. Mydlarski, L. and Z. Warhaft, *On the onset of high-Reynolds-number grid-generated wind tunnel turbulence.* Journal of Fluid Mechanics, 1996. **320**: p. 331-368.
23. Kolekar, N. and A. Banerjee, *Performance characterization and placement of a marine hydrokinetic turbine in a tidal channel under boundary proximity and blockage effects.* Applied Energy, 2015. **148**: p. 121-133.
24. Gad-el-Hak, M. and S. Corrsin, *Measurements of the nearly isotropic turbulence behind a uniform jet grid.* Journal of Fluid Mechanics, 1974. **62**(1): p. 115-143.
25. Hideharu, M., *Realization of a large-scale turbulence field in a small wind tunnel.* Fluid Dynamics Research, 1991. **8**(1-4): p. 53.
26. Makita, H. and S. Miyamoto. *Generation of high intensity turbulence and control of its structure in a low speed wind tunnel*. in *Proceedings of 2nd Asian congress on fluid mechanics*. 1983.
27. Makita, H. *Generation of high intensity turbulence and control of its structure in a low speed wind tunnel*. in *Proc. 2nd Asian Congress on Fluid Mechanics, 1983*. 1983.
28. Poorte, R. and A. Biesheuvel, *Experiments on the motion of gas bubbles in turbulence generated by an active grid.* Journal of Fluid Mechanics, 2002. **461**: p. 127-154.
29. Kolekar, N. and A. Banerjee, *A coupled hydro-structural design optimization for hydrokinetic turbines.* Journal of Renewable and Sustainable Energy, 2013. **5**(5): p. 053146.
30. Mukherji, S.S., et al., *Numerical investigation and evaluation of optimum hydrodynamic performance of a horizontal axis hydrokinetic turbine.* Journal of Renewable and Sustainable Energy, 2011. **3**(6): p. 063105.
31. Selig, M., *Low Reynolds number airfoil design lecture notes.* VKI Lecture Series, November, 2003: p. 24-28.
32. Glauert, H., *Airplane Propellers*, in *Aerodynamic Theory* W.F. Durand, Editor. 1935, Berlin:Springer Verlag.
33. Masters, I., et al., *A robust blade element momentum theory model for tidal stream turbines including tip and hub loss corrections.* Journal of Marine Engineering & Technology, 2011. **10**(1): p. 25-35.
34. Betz, A., *Der Maximum der theoretisch mölichen Ausnützung des Windes durch Windmotoren (The maximum of the theoretically possible exploitation of the wind by wind motors).* Zeitschrift für das Gesamte Turbinenwesen, 1920. **17**(Journal Article).
35. Betz, A., *Windenergie und ihre Ausnutzung durch Windmühen (Wind energy and its application by windmills).* Zeitschrift für das Gesamte Turbinenwesen , Göttingen, 1926(Journal Article).
36. Kolekar, N., et al. *Hydrodynamic Design and Optimization of Hydro-kinetic Turbines using a Robust Design Method*. in *Proceedings of the 1st Marine Energy Technology Symposium, METS13*. 2013. Washington, D.C.

37. Manwell, J.F., J.G. McGowan, and A.L. Rogers, *Wind Energy Explained: Theory, Design and Application*. Vol. 2nd. 2009, New York: John Wiley and Sons.
38. Rae, W.H. and A. Pope, *Low-speed wind tunnel testing*. 1984: John Wiley.
39. Abbott, I.H. and A.E. Von Doenhoff, *Theory of wing sections, including a summary of airfoil data*. 1959: Courier Corporation.
40. Manwell, J.F., J.G. McGowan, and A.L. Rogers, *Wind energy explained: theory, design and application*. 2010: John Wiley & Sons.
41. Kolekar, N., et al. *Hydrodynamic design and optimization of hydro-kinetic turbines using a robust design method*. in *Proceedings of the 1st Marine Energy Technology Symposium METS13*. 2013.
42. Pope, S.B., *Turbulent flows*. 2001: Cambridge University Press.
43. Drela, M. *X Foil subsonic airfoil development system*. http://web.mit.edu/drela/Public/web/xfoil/ 2007.
44. Vinod, A., A.M. Lawrence, and A. Banerjee, *Effects of Free Stream Turbulence on Tidal Turbines. Part II – Turbine Performance and Near Wake Characteristics*, in *EWTEC*. 2017: Cork, Ireland.

Appendix

A. Experimental Setup

The experimental setups for the force measurement experiments and the wake measurement experiments overlap in most aspects. In the wake experiments, there are two elements that must be added to make the measurements appropriately. The base experimental setup consisted of three different parts: the support assembly, the load sensor, and the wing.

The portion of the support structure responsible for changing the setup angle consists of two circular plates, shown below. The upper plate of the setup has a long slot that serves as a guide for plate rotation. The lower plate has two threaded holes. Long bolts are inserted through the slots in the upper assembly and threaded into the holes in the lower assembly. When these bolts are tightened, the two plates are compacted, and the assembly is unable to rotate. When the bolts are loosened, the bottom plate may rotate in either direction for the length of the slot. The slots allow rotation of up to 45 degrees in either direction. For higher angles of attack, the entire assembly must be turned to achieve the correct angles. The wing is fixed securely to the bottom of this rotating setup with two bolts. This entire setup is affixed to the bottom of the Futek load cell (# MTA400).

B. Data Acquisition: Force Measurement

1. Plug three Futek sensor USBs into three ports on the computer. Open the Futek software, Sensit.
2. With another person, determine which reading corresponds to which direction. This can be done by applying pressure to the leading edge of the wing and watching for an increase in one reading (data channels that must be read may be seen in figure 21). This reading represents the drag on the wing. To find the lift, apply force to either the suction or pressure side of the wing. The final reading is the force in the Z direction and will not be used in this experiment.
3. Right click on each of these readings and select "tare." This zeros the sensor and allows for unbiased measurement.
4. Click on the "Data Logging Mode" tab. Click Settings, select USB and enable all devices. Enter the test duration and click "Ok."
5. Perform a residue test. To do this, keep the tunnel and grid off and take measurements for 15 seconds. Click "File Path" to name the test, and then click "Start Test."
6. Start the tunnel, and run the grid if the test necessitates. Click "File Path" to name the test, and then click "Start Test."
7. Perform all necessary tests.

C. Data Acquisition: Wake Measurement Experiments

1. Plug Vectrino ADV into the computer, and supply with power.
2. *Open Vectrino software. Ensure all settings match those indicate in figure 23. These are the settings that allow the ADV to perform appropriately in this environment. Apply changes and click "OK."*
3. At this point, the tunnel and grid should be started to begin the experiment. For further information and instruction about these processes, please refer to Appendix E.
4. Select the "Data Collection" drop-down menu. Within this menu, click "Data Recording." A window will open that looks like figure 24 Choose the desired location for the data and name the file. At this point, the time may be adjusted according to the test. Each wake measurement test was run for 30 seconds. (After convergence studies that allowed 10 minutes of data collection, it was discovered that results converged at 30 seconds, so only 30 seconds of data were required.)
5. Click "OK" and exit this window. Before testing may begin, it is crucial at this point to check the correlation percentage. This acts as an indicator of the reliability of the data. If the correlation drops below 80%, particles should be added to the water to increase the number of surfaces off of which the acoustic signal the ADV sends may reflect. Figure C3 includes an image of the user interface used in the software, with an indication as to where the correlation is.

6. Once the correlation is at appropriate levels, click the “Data Collection” drop-down menu, and select “Start Collection.” Allow the test to run to completion.
7. Repeat steps 5 and 6 until all tests have been performed. When finished, click the “Data Collection” drop-down menu, and select “Data Conversion.” This will open the window seen in figure C4. Click “Add File” and choose all files that need to be processed. Once in the window, click “Select all” and click the blue arrow to convert into a usable file format.

D. Standard Operating Protocol: Force Measurement

When taking load measurements, it is crucial that

As a result, the following steps are followed in performing each set of measurements. This ensures that all measurements are consistent.

1. Adjust wing angle of attack to zero before lowering wing into the tunnel or making any measurements. This ensures that there is less imbalance in the weight of the system, which makes it easier to set up.
2. Rest metal supports on either side of the tunnel. Keep the blade in the air (out of the tunnel) straight up.
3. 10 mesh sizes downstream (40 inches). Mark this spot with a piece of tape on both sides of the tunnel.
4. Slowly lower blade into the tunnel, with metal, supports resting on either side of the water tunnel. Ensure that the leading edge of the blade is aligned with the mark on the side of the tunnel.
5. Once the leading edge is in the correct position, measure the position of the metal brackets on either side of the tunnel. These will need to be equidistant from the front of the grid. Align these accordingly while maintaining the position of the leading edge.
6. Measure from one wall of the tunnel to the leading edge of the blade. This distance should be half of the tunnel width, which is 24 inches. While maintaining the downstream location, push the metal support bracket flush to the side of the tunnel that allows for the leading edge to be 12 inches from either wall.

7. Clamp down all four brackets. Clamps should be applied loosely on all points before they are tightened.
8. Set the angle of attack according to pre-marked setup. The angle of attack may be adjusted by loosening (not removing) bolts in two-disk setup and turning lower disk and wing to the appropriate angle.
9. Check that water level in the tunnel is at 23 and 7/16 inches, which is the standard height at which all experiments are performed.
10. Collect 30 seconds of sensor measurement while the tunnel is still off. This will serve as a residue measurement and allows for an adjustment to ambient conditions.
11. Turn tunnel on to appropriate operating frequency. Wait until tunnel has reached velocity indicated.
12. If experiments are using the grid Single Random or Double Random protocols, start the grid.
13. Collect force measurement data for two minutes. Turn off grid and tunnel.
14. Repeat steps 8 through 13 for every angle of attack measurement desired.

E. Standard Operating Protocol: Wake Measurement

Wake measurements prove somewhat tricky in the environment produced the nature of these tests. This is due to the facts that the flow is made to simulate some of the more difficult conditions that turbines will face and that the tunnel available to us is only .6096 meters by .6096 meters. The blade must be quite small to negate the effects of blockage and is less structurally stable as a result. The following instructions outline an appropriate protocol for taking wake velocity measurements behind a wing in the tunnel used in these experiments. This includes attaching a suction cup to the bottom of the wing to prevent any bending that may skew the results of the test, and place an ADV in the water directly behind the wing.

Part 1: Blade Setup

1. Insert the upstream headwall according to grid operation protocol. Use the valve in the grid section to drain the test section of the tunnel. The rest of the tunnel will remain filled with water.
2. Swap metal rod in the center of the wing with another, slightly longer one. This rod had the ability to pass through a hole drilled in the middle of the suction cup handle. Secure a nut on the bottom of the now-attached suction cup. Tighten the bolt, but not enough that the wing will not be able to rotate when the suction cup is secured to the bottom of the tunnel.
3. Adjust wing angle of attack to zero before lowering wing into the tunnel or making any measurements. This ensures that there is less imbalance in the weight of the system, which makes it easier to set up.

4. Rest metal supports on either side of the tunnel. Keep the blade in the air (out of the tunnel) straight up.
5. 10 mesh sizes downstream (40 inches). Mark this spot with a piece of tape on both sides of the tunnel.
6. Slowly lower blade into the tunnel, with metal, supports resting on either side of the water tunnel. Metal supports will need to be supplemented with additional padding underneath, to account for the height of the suction cup. Ensure that the leading edge of the blade is aligned with the mark on the side of the tunnel.
7. Once the leading edge is in the correct position, measure the position of the metal brackets on either side of the tunnel. These will need to be equidistant from the front of the grid. Align these accordingly while maintaining the position of the leading edge.
8. Once the entire system is appropriately aligned, slide a thin spacer under the metal bracket on either side to elevate the system enough to remove the plastic covers from the suction cup.
9. Remove the suction cup covers and position the handle parallel to the grid (perpendicular to the wall of the tunnel). Remove temporary spacers and allow suction cup handle to secure to the floor of the tunnel. Flatten the levers on top of the suction cup. This will now be firmly secured to the ground.
10. Slowly clamp the four metal brackets supporting the system.
11. Once the wing is positioned appropriately in the tunnel, the tunnel should be refilled to the position of 23 and 7/16 inches. At this point, the headwall should

be removed for laminar experiments. For grid experiments, the downstream headwall should be inserted appropriately, and other processes for inserting the grid should be followed.

12. Adjust the angle of attack to an appropriate level for the test.

Part 2: ADV Setup

13. Using hose clamp, mount ADV on rack assembly. With the ADV used in these experiments, be sure that the prongs are positioned such that they are all facing the wall of the tunnel. Hose clamp should nestle in the thick indent on ADV. ADV should be secured as tightly as possible.
14. Make markings with tape on the tunnel for the necessary measurement positions. In our case, this was 2 chord lengths and 4 chord lengths down-stream of the wing.
15. Ensure that the ADV is locked in place by tightening the black lever on its carriage. If the ADV slides, the setup will become more difficult to place in the tunnel appropriately and could be dangerous to the ADV.
16. With two people, lift the ADV support structure into the tunnel, being careful not to let the ADV hit anything as it is moved. The structure should go behind the wing, with the ADV closer to the front of the tunnel.
17. Align the center of the ADV measurement probe with the first measurement location on the tunnel. Clamp the metal supports on either side lightly.
18. Measure the distance from the grid to the metal support on either side. Adjust until these distances are even while maintaining the position of the probe.

19. Clamp the ADV setup tightly on both sides of the tunnel. Slide the ADV so that the line on the carriage is aligned with the ruler's 0" mark on the rail.
20. Follow the procedure outlined for data acquisition in Appendix B.
21. Move the ADV to the next measurement position. If measuring in half-inch increments, move the ADV ½ inches to the right by aligning carriage line with ruler line.
22. Continue until all cross-tunnel measurements have been taking. Do not measure within two inches of the tunnel wall.
23. Continue adjusting the angle of attack to appropriate test level and adjusting the grid protocols according to test conditions. Repeat steps 16-19 to move the ADV to the next measurement location.

F. BEM Code

```
% Written by Nitin Kolekar
% Commented by Matthew Pasch Fall 2016
% Further commenting and simplification done by Angela Lawrence Fall
% 2017
% BEM to find COP for a given blade geometry
% MHKE application
% Fall 16

clc
clear all
close all
format long

% define all constants as matrices of zeros
phi=zeros;Lr=zeros;sigma=zeros;a=zeros;ap=zeros;V_rel=zeros;
Re=zeros;Cl=zeros;Cd=zeros;alfa=zeros;Fact=zeros;f_tip=zeros;
F_tip=zeros;f_hub=zeros;F_hub=zeros;F=zeros;delta_a=zeros;
Cn=zeros;Ct=zeros;K=zeros;T=zeros;Q=zeros;omega=zeros;A=zeros;
AP=zeros;ALFA=zeros;FF=zeros;CL=zeros;CD=zeros;Cp=zeros;PHI=zeros;
Coef_of_Per=zeros;gamma = 0;

r_hub = .0127;                % define hub radius (m)
R=0.127;                      % Radius (m)

L = 1:0.5:7;                  % define range of TSR

B=3;                             % # of blades
rho=998;                         % water density
U=0.73;                          % free stream velocity
mu=10.16E-4;                     % water viscosity
RPM=60*L*U/(2*pi*R);             % rpm
P_in=0.5*rho*pi*R^2*U^3;         % power in the wind


%% TSR Loop %%
for g = 1:length(L)

    omega(g)=(L(g)*U)/R;         % rotational velocity

    %radius points at each element


%r=[0.029104167;0.029104167;0.034925;0.040745833;0.046566667;0.052387
5;0.058208333;0.064029167;0.06985;0.075670833;...
  %
0.081491667;0.0873125;0.093133333;0.098954167;0.104775;0.110595833;0.
116416667;0.1222375;0.128058333;0.133879167;0.1397];

  [r] = .04:(R-.04)/20:R;

    theta_p0 = ones(length(r),1)*deg2rad(1);           % blade pitch
angle at the tip
```

```
    c = ones(length(r),1)*0.0193548;                          % cord
length (constant cord)
    theta_t = ones(length(r),1)*0*pi/180;                 % blade twist
angle (zero twist)
    theta_p = theta_t+theta_p0;                               % section
pitch angle

    o=1;


%% Summation over 'N' number of blade elements %
 for i=1:length(r)
       Lr(i,1) = L(g)*r(i)/R;                            % local TSR
       sigma(i,1) = B*c(i)/(2*pi*r(i));                  % local solidity


       %Re BASED on CHORD

       Re_ref = 12018;

       a(i,1)=0.0;       % local axial induction factor initialization
       ap(i,1)=0.0;      % local angular induction factor
initialization


       z = 0;            %initialization

        if(i>1)
            a(i,1)=a(i-1,j+1);
            ap(i,1)=ap(i-1,j+1);
        end

       % iteration to find axial (a) and angular (ap) induction
factors

       j=1;

 while (z==0)

            phi(i,j) = atan((1-
a(i,j))*U/((1+ap(i,j))*omega(g)*r(i)));          %angle of relative
wind Manwell 3.63

            V_rel(i,j)=sqrt((U*(1-
a(i,j)))^2+(r(i)*omega(g)*(1+ap(i,j)))^2);    %vector combination of
velocity components

            Re(i,j)=rho*V_rel(i,j)*c(i)/mu;
%Correction for Reynolds number

            Fact(i,j)=(Re_ref/Re(i,j))^0.2;
%calculation for final state of C_d = C_d*Fact

            alfa(i,j)=((phi(i,j)-theta_p(i)))*180/pi;
%calculation of angle of attack Manwell 3.62
```

```
%% Lift and Drag Reference Section from XFoil

%Angela Data SG6043
alfa1 = [   -40 -35 -30 -25 -20 -15 -10 -5  0   5   10  13  15  17
20  25  30  35  40  ];
Cd1 = [ 1.43635153  1.083476755 0.857650272 0.678445312 0.490807614
0.379844676 0.291133763 0.149114575 0.057468921 0.041086378
0.080203878 0.12656536  0.140979026 0.166128645 0.366322577
0.578552663 0.801370107 1.044173511 1.278581326 ];
Cl1 = [ -1.259449784    -1.137490853    -1.032731735    -0.926598117
-0.771428317    -0.692338897    -0.64070231 -0.371077601
0.124002105 0.807202441 1.415659746 1.693197113 1.733614816
1.765934118 1.576773327 1.624509308 1.623209106 1.698026434
1.757092746 ];


%interpolation to find appropriate angle of attack from reference
data

alfa1i = alfa(i,j);
Cl(i,j) = interp1(alfa1,Cl1, alfa1i,'pchip');
Cd(i,j) = interp1(alfa1,Cd1, alfa1i,'pchip');


%Cd(i,j)=Cd(i,j)*Fact(i,j);                                  %correction
from Nitin paper Formula (1)


%Components in Normal and Tangent directions from phi

Cn(i,j)=Cl(i,j)*cos(phi(i,j))+Cd(i,j)*sin(phi(i,j));
Ct(i,j)=Cl(i,j)*sin(phi(i,j))-Cd(i,j)*cos(phi(i,j));


%tip losses Manwell 3.128

f_tip(i,j)=(B/2)*(R-r(i))/(r(i)*sin(phi(i,j)));          %inside cos
F_tip equation
F_tip(i,j)=2/pi*acos(exp(-f_tip(i,j)));                  %final
calculation F_tip equation

%hub losses Nitin, Aerodyn Theory Manual [13]

f_hub(i,j)=(B/2)*(r(i)-r_hub)/(r_hub*sin(phi(i,j)));     %inside cos
F_Hub equation
F_hub(i,j)=2/pi*acos(exp(-f_hub(i,j)));                  %final
calculation F_hub

F(i,j)=F_tip(i,j)*F_hub(i,j);                            %combined tip
and hub correction factor
```

```
 a(i,j+1)=1/((4*F(i,j)*(sin(phi(i,j)))^2/(sigma(i)*Cn(i,j)))+1);
%axial induction factor with tip & hub correction 3.131 Manwell

 K(i,j)=4*F(i,j)*(sin(phi(i,j)))^2/(sigma(i)*Cn(i,j));
%simplifying number

              if (a(i,j+1)>0.2)

              a(i,j+1)=0.5*(2+K(i,j)*(1-2*0.2)-sqrt((K(i,j)*(1-
2*0.2)+2)^2+4*(K(i,j)*0.2^2-1)));        %reference?

              end


              CT(i,j+1)=(1-
a(i,j+1))^2*sigma(i)*Cn(i,j)/(sin(phi(i,j)))^2;
%local thrust coeff. Manwell 3.130



ap(i,j+1)=1/(4*F(i,j)*sin(phi(i,j))*cos(phi(i,j))/(sigma(i)*Ct(i,j))-
1);                  %Manwell 3.133
              delta_a(i,j)=a(i,j+1)-a(i,j);
%tolerance of a
              temp1=abs(delta_a(i,j));
%absolute tolerance of a

              if temp1>=0.0001
% specifying tolerance
                 z=0;
              if(i>=2)
                   a(i,j+1)=0.8*a(i,j)+0.2*a(i,j+1);
%reference? Final a
                  %a(i,j+1)=0.5*a(i,j)+0.5*a(i,j+1);
              end
                j=j+1;
%next iteration
              else
                z=1;
%finishes iterative calculation of a and ap
              end
           o=o+1;
 end
 %%
 % Using the corrected values of induction factors to find Cp %


 %initializing variables from previous section
        A(i)=a(i,j);
        AP(i)=ap(i,j);
        PHI(i)=phi(i,j);
        FF(i)=F(i,j);
        CL(i)=Cl(i,j);
        CD(i)=Cd(i,j);
```

```
        ALFA(i)=alfa(i,j);

        DELTA_A(i)=delta_a(i,j);
        RE(i)=Re(i,j);
        CT1(i)=CT(i,j+1);


        Cp(i)=FF(i)*(sin(PHI(i)))^2*(cos(PHI(i))-
Lr(i)*sin(PHI(i)))*(sin(PHI(i))+Lr(i)*cos(PHI(i)))*(1-
(CD(i)/CL(i))*cot(PHI(i)))*(Lr(i))^2; %Cp equation Manwell 3.91a



        dr=R/length(r);
        T(i)=FF(i)*rho*U^2*4*A(i)*(1-A(i))*pi*r(i)*dr;
% Axial Force Manwell 3.58a
        Q(i)=4*FF(i)*AP(i)*(1-A(i))*rho*U*pi*(r(i))^3*omega(g)*dr;
% Torque 3.59a

        ForceA(i)=CT1(i)*0.5*rho*U^2*2*pi*r(i)*dr;

end


%    Force(g)=sum(T);
%    Torque(g)=sum(Q);
%    TSR=L(g)
%    ALFA

   Coef_of_Per(g)=8*sum(Cp)/(L(g)*(length(r)));
   Torque(g)=Coef_of_Per(g)*P_in/omega(g);
   Force(g)=sum(ForceA);
   SIGMA=B*c(1)*R/(pi*R^2);
% Turbine solidity

   Coef_of_Thrust(g)=Force(g)/(0.5*rho*pi*R^2*U^2);

end

 COP=transpose(real(Coef_of_Per));
 COT=transpose(Coef_of_Thrust);
 PERF=transpose(COP);
 SIGMA;
 [maxCOP, w] = max(COP);
 P_out_max=P_in*maxCOP;

%plotting

figure (1)
subplot (2,1,1)
plot(L,COP);xlabel('TSR');ylabel('C_P');
hold all

%figure(2)
subplot (2,1,2)
```

```
plot(L,COT);xlabel('TSR');ylabel('C_T');
hold all

chord=c(1);
tipspeedratio=transpose(L);
ForceT=transpose(Force);

Q = [L', COP];
fprintf('Max C_P  = %.4f at %.0f TSR',maxCOP,L(w));
```

Vite

Angela Lawrence first became interested in engineering when she was in 8th grade, at which point she began a high school engineering program. Since then, she has completed internships with Harry E. Cole and Son Civil Engineering Firm, United Technologies Aerospace Systems, and Ingersoll Rand (Power Tool Division). She has also completed her undergraduate degree in Mechanical Engineering in the Lehigh University Class of 2016. Through her graduate career, Angela has won third place in the Young Engineers Paper Competition and has presented at the European Wave and Tidal Energy Conference. She was awarded the National Science Foundation Graduate Fellowship in 2017.. She will be starting work at Intelliquip in Bethlehem, PA after graduation.